Fabrication of superhydrophobic CNF/PVA composite aerogel for oil/water separation

Y. H. Xu, Y. Y. Han, H. Y. Li, J. Yang, B. Q. Fu, H. F. Zhao*, L. Z. Sha, T. Z. Yuan
School of Environmental and Natural Resources, Zhejiang University of Science and Technology, Hangzhou 310023, China

Aerogel has received increasing attention in oily wastewater treatment due to its high porosity, low density and good absorption capacity. In this work, the biodegradable bleached softwood pulp was used to prepare three distinct cellulose nanofibrils via high-pressure homogenization (CNF), integrating enzymatic pretreatment and TEMPO-oxidation with high-pressure homogenization (ECNF and TCNF), and the corresponding CNF aerogels were fabricated and hydrophobically modified by stearoyl chloride (SAC). Subsequently, the CNF optimized based on oil absorption was crosslinked with polyvinyl alcohol (PVA) to prepare CNF/PVA composite aerogel with good physical properties. The results showed that the hydrophobically modified SAC-TCNF/PVA composite aerogel exhibited ultralow density (15.2 $mg \cdot cm^{-3}$), ultrahigh porosity (99.0%) and superhydrophobicity (with a water contact angle of 150.4°) when the ratio of TCNF to PVA was 1:0.5. Remarkably, the SAC-TCNF/PVA composite aerogel displayed high elastic recovery rate of 59.5% after five rebound tests, high cyclic oil absorption capacity of 31.6 $g \cdot g^{-1}$ in the fifth cycle, which was the 69.7% of the initial oil absorption capacity, demonstrating its excellent physical properties and recyclability in oil-water separation.

(Received July 15, 2025; Accepted October 15, 2025)

Keywords: Cellulose nanofibril (CNF), Composite aerogel, Superhydrophobicity, Oil-water separation, Recyclability

1. Introduction

With the acceleration of industrialization, oily wastewater generated from petrochemical, transportation, pharmaceutical, and food industries has posed severe environmental threats, particularly in marine oil spill incidents where ecological damage is profoundly alarming [1-3]. Therefore, the development of efficient oil-water separation technology to mitigate environmental pollution and protect water resources has become a global challenge and research hotspot. Aerogel is a porous material with high porosity, low density, large specific surface area and excellent adsorption, and widely used in water pollution treatment, thermal insulation, energy storage, and biomedical fields [4-7]. Cellulose-based aerogels are known as the third-generation aerogel materials following inorganic and organic polymer aerogels, characterized by eco-friendliness and biodegradability [8]. Cellulose nanofibril (CNF) is a type of cellulose material with nanoscale dimensions, aerogels prepared with CNF not only possess low density, high porosity and renewability but also have high mechanical strength and ease of chemical modification, showing significant application potential in adsorption and oil-water separation [9,10].

CNF can be prepared through mechanical methods [11], chemical methods [12], and pretreatment-assisted mechanical approaches [13,14]. The dimensions, functional groups and properties of CNF vary depending on the preparation method, which in turn influences the structure and performance of the resulting nanocellulose aerogels [15]. Wang et al. [16] fabricated CNF with a diameter of 50-70 nm through mechanical grinding, and the density, specific surface area and porosity of the resulting CNF aerogel prepared by lyophilization were 54.2 $mg \cdot cm^{-3}$, 176 $m^2 \cdot g^{-1}$ and 97.2%, respectively. In comparison, the CNF prepared by integrating TEMPO-mediated oxidation with high-pressure homogenization (named as TCNF) showed a smaller diameter of 3-4

* Corresponding author: zhf9966@163.com
https://doi.org/10.15251/DJNB.2025.204.1297

nm, and the CNF prepared by integrating enzyme pretreatment with high-pressure homogenization (named as ECNF) displayed a diameter of 10-40 nm [17,18]. Gong et al. [19] incorporated styrene-acrylic emulsion (SAE) into TCNF to fabricate nanocellulose aerogel, and the resulting aerogel had a low density of 10.3-11.7 $mg \cdot cm^{-3}$, a high specific surface area of 184 $m^2 \cdot g^{-1}$ and an ultrahigh porosity of 99.0%, demonstrating great potential in water pollution treatment. Although nanocellulose aerogels generally exhibited high porosity and excellent adsorption capacity, their poor mechanical strength and hydrophobicity limited their practical application in oil-water separation. Reports indicated that incorporation of crosslinking agent or hydrophobic modification could effectively enhance the mechanical properties and hydrophobicity of nanocellulose aerogels [20,21]. Yahya et al [22] prepared CNF aerogel using ECNF and modified it with triethoxymethyl silanes (TEMS), and the resulting aerogel had a water contact angle (WCA) of 136.2° and an edible oil absorption capacity of 44.3 $g \cdot g^{-1}$, showing a broad application prospects in the field of oil-water separation. He et al. [23] prepared an enhanced cellulose aerogels by incorporating aluminate hydrate nanoparticles as crosslinking agent. Rafieian et al. [24] fabricated a hydrophobic nanocellulose aerogel by vapor-phase deposition of silane coupling agents.

In this work, bleached softwood pulp was used as raw material to prepare cellulose nanofibril through high-pressure homogenization (CNF), enzymatic pretreatment and Tempo-oxidation integrating with high-pressure homogenization (ECNF and TCNF), and the corresponding CNF aerogels were fabricated and hydrophobically modified by stearoyl chloride (SAC). Subsequently, the CNF optimized based on oil absorption was crosslinked with PVA to prepare CNF/PVA composite aerogel with high mechanical strength and oil absorption capacity, and the optimal composite process and the oil-water separation efficiency of the composite aerogel were investigated.

2. Experimental

2.1. Experimental materials

Bleached softwood pulp was obtained from Chile, (Brazil). Cellulase (enzyme activity: 500 U/mL) was purchased from Hangzhou Xilikang Chemical Co., Ltd. (China). Sodium hypochlorite (NaClO, CP), sodium bromide (NaBr, AR), sodium hydroxide (NaOH, AR), n-hexane, 6-Tetramethylpiperidin-1-oxyl (TEMPO, AR) and acetonitrile (AR) were all purchased from Shanghai Lingfeng Chemical Reagent Co. Ltd. (China). Polyvinyl alcohol (PVA) and stearoyl chloride (SAC) were provided by Shanghai Aladdin Reagent Co., Ltd. (China). Triethylamine was purchased by Chengdu Kelong Chemical Co., Ltd. (China).

2.2. Experimental method

2.2.1. Preparation of nanocelluloses

Bleached softwood pulp was dispersed into water and agitated to form homogeneous pulp suspension, then the suspension was diluted and processed in a microfluidizer high-pressure homogenizer (Microfluidics International Corporation, USA) at 20,000 psi for 30 cycles to obtain a nanocellulose product, designated as cellulose nanofibrils (CNF) [20]. At the same time, the dispersed pulp suspension was respectively pretreated by cellulase enzymatic hydrolysis and TEMPO-mediated oxidation, and then processed in the high-pressure homogenizer to yield two types of nanocellulose products, and respectively designated as enzyme pretreatment cellulose nanofibrils (ECNF) and TEMPO-mediated oxidation cellulose nanofibrils (TCNF) [21,23].

2.2.2. Preparation and hydrophobic modification of nanocellulose aerogels

Three types of nanocellulose aerogels were respectively fabricated in a freeze dryer (SCIENTZ-10N, Ningbo Scientz Biotechnology Co., Ltd, China) using the prepared CNF, ECNF and TCNF as the raw materials. Meanwhile, 0.1 mol/L stearoyl chloride (SAC) solution was prepared by adding 1 mL SAC and 40 μL triethylamine into 30 mL acetonitrile. Subsequently, the prepared aerogels were immersed in the SAC solution for 1 h to yield hydrophobic nanocellulose aerogels.

Among the three types of nanocelluloses, one of the optimal nanocellulose product was selected for later use based on comparative evaluation of their oil/water separation performance after hydrophobic modification.

2.2.3. Preparation and hydrophobic modification of nanocellulose/PVA composite aerogels

A certain amount of solid PVA was dissolved into deionized water at 90 °C under continuous stirring. Subsequently, 12.5 g (1.2 wt%) of the selected nanocellulose was mixed with PVA solutions to obtain nanocellulose/PVA mixtures, and the component of the mixtures was precisely controlled as detailed in Table 1.

Table 1. The composition of nanocellulose/PVA composite aerogels.

Nanocellulose: PVA	Nanocellulose/g	PVA/g	H_2O/g	Total/g
1:0	12.5	0	17.5	30
1:0.5	12.5	0.075	17.425	30
1:1	12.5	0.15	17.35	30
1:1.5	12.5	0.225	17.275	30
1:2	12.5	0.3	17.2	30

The mixtures were sonicated for 30 min using an ultrasonic cleaner, followed by constant-speed magnetic stirring at 500 rpm for 6 h, and the nanocellulose/PVA composite aerogels were fabricated based on freeze-drying using the well-mixed nanocellulose/PVA systems as raw materials. Whereafter, the nanocellulose/PVA composite aerogels were hydrophobically modified in the same way as nanocellulose aerogels, and the finished products were designated as SAC-nanocellulose/PVA composite aerogels. The schematic diagram of the preparation of SAC-nanocellulose/PVA composite aerogel was shown in Fig.1.

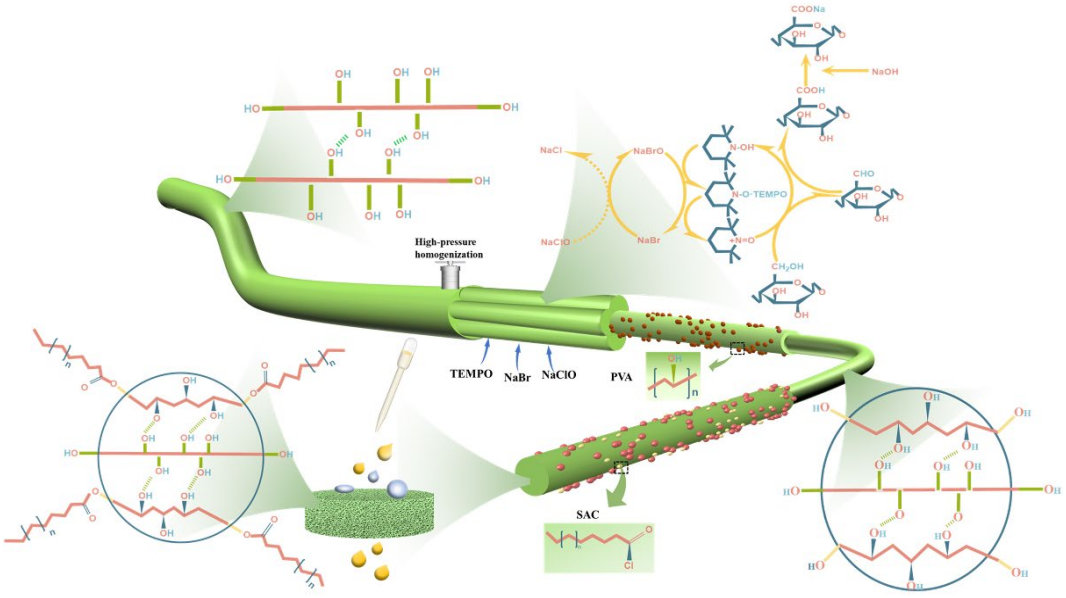

Fig. 1. Schematic diagram of the preparation of SAC-nanocellulose/PVA composite.

2.2.4 Nanocellulose analysis

The CNF, ECNF and TCNF samples were dried, ground and pelletized using KBr, and the FT-IR spectra of them were recorded in the range of 500-4000 cm^{-1} with a resolution of 4 cm^{-1} on an infrared spectrometer (FTIR-8400S, Shimadzu, Japan). The X-ray diffraction pattern of the samples was obtained in a 2θ range between 0 and 80° using an X-ray diffractometer (Ultima-IV, Kuraray, Japan) at a scanning rate of 5°·min^{-1}, and their crystallinity indexes (*CrI*) were calculated as Eq. (1) [25].

$$CrI = \frac{(I_{200} - I_{am})}{I_{200}} \times 100\% \quad (1)$$

where I_{200} was the intensity of the diffraction peak at 2θ = 22.5° and I_{am} was the diffraction intensity minimum corresponds to the peak at 2θ = 18°.

The morphological characteristics of CNF, ECNF and TCNF were observed and their diameter and length were determined by using atomic force microscope (AFM, Dimension Icon, Bruker, Germany) [26]. Zeta potential of the nanocellulose suspensions (2 mg·mL^{-1}) were measured using a nanoparticle analyzer (Nano-ZS, Malvern Instruments, UK) at 25 °C. The Turbiscan Stability Index (TSI) of CNF, ECNF, and TCNF suspensions (0.5 wt%) were analyzed using a multiple light scattering analyzer (Turbiscan Lab, Formulaction, France), and the samples were scanned at 30 min intervals over 180 min. Thermogravimetric measurements were performed using a simultaneous thermal analyzer (TA instruments, SDT-650, USA) from room temperature to 800 °C at a heating rate of 10 °C·min^{-1} under nitrogen atmosphere (50 mL·min^{-1}).

2.2.5. Aerogels analysis

The dry and wet tensile strength of the paper samples were determined according to TAPPI 404 and TAPPI 456 protocols. The burst and tear strength of the samples were determined according to TAPPI 403 and TAPPI 414 protocols [2]. All these tests were repeated in triplicate. FT-IR spectra of the aerogels were recorded on the FTIR-8400S infrared spectrometer. The morphologies of the aerogels were observed using a scanning electron microscope (SEM, SU1510, Hitachi, Japan) at an accelerating voltage of 15 kV [27]. The thermogravimetric measurements of the aerogels were carried out using SDT-650 simultaneous thermal analyzer. The apparent density and porosity of the aerogels were calculated according to the Eq. (2) and Eq. (3) [28].

$$\rho = \frac{m}{v} \quad (2)$$

$$P = \frac{\rho - \rho_c}{\rho} \times 100\% \quad (3)$$

where ρ was the density of the aerogel, mg·cm^{-3}; m was the mass of the aerogel, mg; v was the volume of the aerogel, cm^3; P was the porosity of the aerogel, %; ρ_c was the density of the fiber skeleton and ρ_c = 1.528 g·cm^{-3}.

The water wettability of the aerogels was measured using a contact angle analyzer (DSA30, KRÜSS, Germany), and the droplet volume was set as 5 μL. The oil absorption capacity of the aerogels was measured by immersing the sample in edible oil for 30 mins until it was completely saturated and calculating according to the Eq. (4) [29].

$$Q = \frac{m_2 - m_1}{m_1} \quad (4)$$

where m_2 was the mass of aerogel saturated with oil, g; m_1 was the mass of the aerogel without oil, g; and Q was the adsorption capacity per gram of the aerogel, g·g^{-1}.

The SAC modified aerogel was immersed in the oil-water mixture to determine its oil-water separation effect, and the oil-water separation efficiency (P) was calculated according to the Eq. (5).

$$P = \frac{m_4 - m_3}{m} \times 100\% \quad (5)$$

where m_4 was the mass of the aerogel after oil absorption, g; m_3 was the mass of the aerogel before being placed into the oil-water mixture, g; m was the mass of oil in the oil-water mixture, g.

After being soaked in edible oil for 30 mins, the SAC modified aerogel was taken out and reused for oil absorption after being squeezed, washed with n-hexane and freeze-dried. After five cycles of regeneration, the oil absorption capacity was used to evaluate the cyclic oil absorption performance of the aerogel. Elastic recovery of the aerogels was tested using a ball-drop resilience tester (HS-1002, Shanghai Hesheng Instruments Co., Ltd., China). A steel ball was dropped freely from a certain height and touched the surface of the aerogel sample (Φ40 mm×10 mm), then the height the ball bounced up was measured to evaluate the elastic properties of the aerogels. The elastic recovery rate of the aerogels was calculated according to the Eq. (6) [30].

$$R_g = \frac{H_2}{H_1} \times 100\% \tag{6}$$

where R_g was the elastic recovery rate, %; H_1 was the falling height of the steel ball, mm; H_2 was the rebound height of the steel ball, mm.

3. Results and discussion

3.1. Morphology and properties of nanocelluloses

AFM images and the size characteristics of three different nanocelluloses were shown in Fig.2(a) and Fig.2(c). Comparative analysis revealed a distinct fiber morphology distribution where CNF displayed the largest fiber diameter and length, ECNF showed the shortest fiber length while TCNF displayed the smallest fiber diameter. The preparation of CNF relying solely on mechanical homogenization resulted in larger fiber bundles with noticeable flocculation, attributed to insufficient disruption of strong intermolecular hydrogen bonds that led to incomplete defibrillation and fiber aggregation [31]. In contrast, enzymatic pretreatment in ECNF production selectively degraded amorphous regions of cellulose, facilitating more effective mechanical disintegration during subsequent homogenization and yielding finer fibrils [32]. The TEMPO-oxidation approach for TCNF preparation converted the hydroxyl groups to carboxylate groups, effectively cleaving the hydrogen bonds between cellulose macromolecules, thereby producing nanofibrils with the most uniform and reduced diameters [33]. This proved the preparation method-dependent morphology characteristics of nanocelluloses.

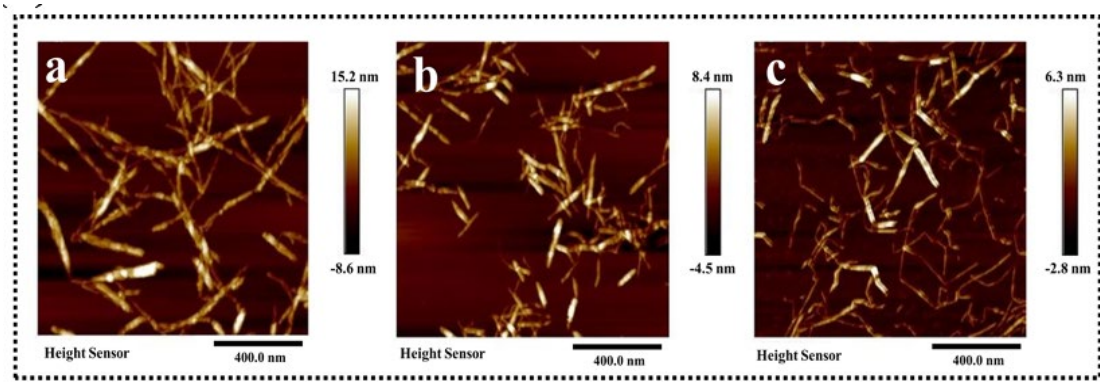
a
15.2 nm
-8.6 nm
Height Sensor
400.0 nm
b
8.4 nm
-4.5 nm
Height Sensor
400.0 nm
c
6.3 nm
-2.8 nm
Height Sensor
400.0 nm

(a)

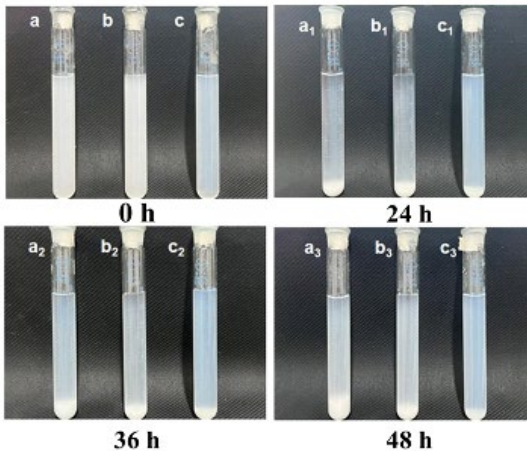
a
b
c
0 h
a1
b1
c1
24 h
a2
b2
c2
36 h
a3
b3
c3
48 h

(b)

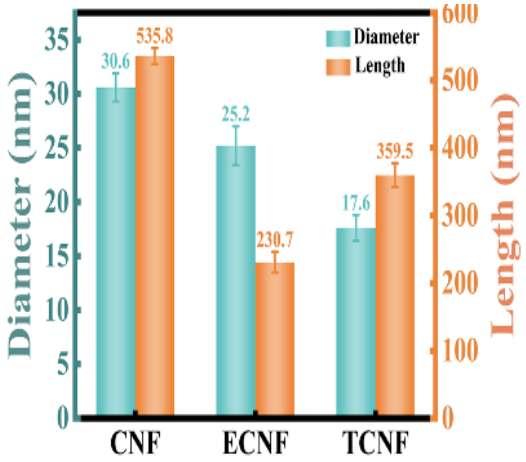
Diameter
Length
Diameter (nm)
Length (nm)
30.6
535.8
25.2
230.7
17.6
359.5
CNF
ECNF
TCNF

(c)

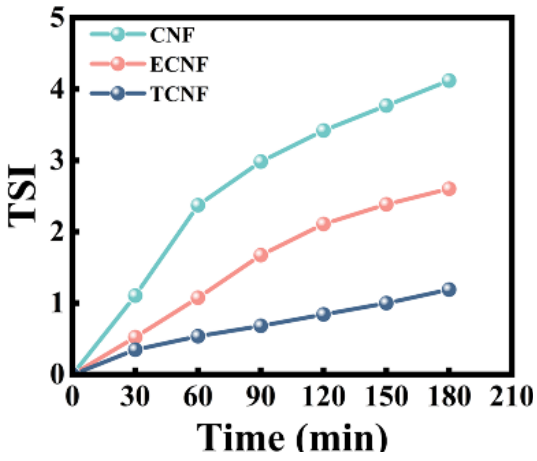
CNF
ECNF
TCNF
TSI
Time (min)

(d)

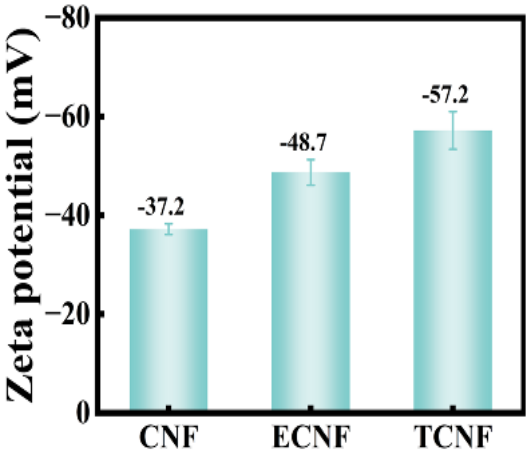
Zeta potential (mV)
-37.2
-48.7
-57.2
CNF
ECNF
TCNF

(e)

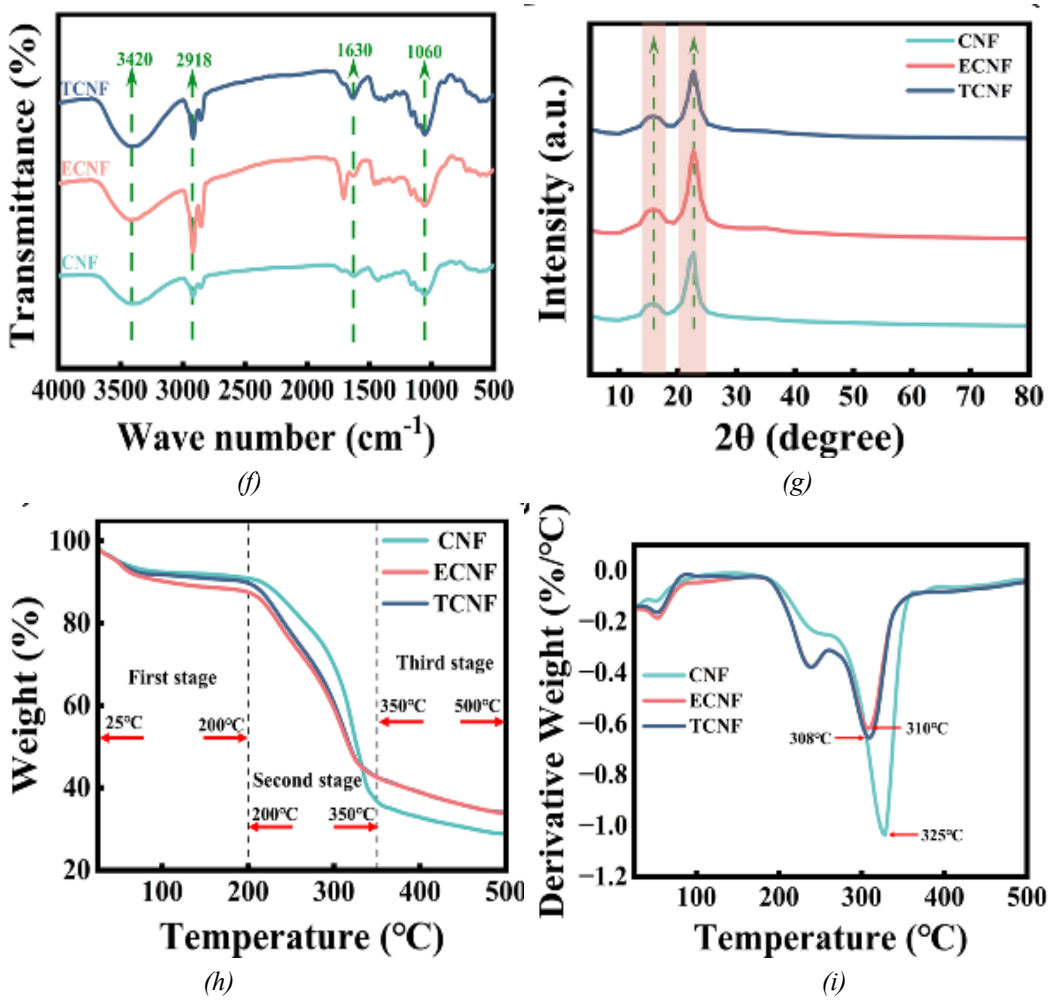

Fig. 2. Morphologies and properties of three kinds of nanocelluloses (a) AFM plots of nanocelluloses; (b) Photos of nanocellulose suspensions (0.5 wt%); (c) Diameter and length of nanocelluloses; (d) Dispersion stability of nanocelluloses; (e) Zeta potential of nanocelluloses; (f) FT-IR spectra of nanocelluloses; (g) XRD pattern of nanocelluloses; (h) TG curve and (i) DTG curve of nanocelluloses.

Fig.2(b) compared the sedimentation behavior of the three nanocellulose suspensions (0.5 wt%) after 24 h, 36 h, and 48 h static storage at 25 °C. All nanocellulose suspensions showed sedimentation and stratification phenomena with the extension of the standing time. It was found that the sedimentation degree of CNF was the greatest and that of TCNF was the smallest, and the differences in sedimentation behavior resulted from the morphology differences of nanocelluloses. The larger fibrils and stronger inter-fibrillar bonding promoted aggregation and sedimentation of CNFs, while smaller fibrils and more exposed hydroxyl groups enhanced colloidal stability of TCNF via hydrogen bonding. The TSI of nanocellulose suspensions over 180 mins were showed in Fig.2(d). The lower the TSI, the more stable the nanocellulose suspensions [34]. CNF exhibited the highest TSI while TCNF maintained the lowest TSI over 180 mins, indicating CNF had the poorest stability and TCNF was the most stable one. The zeta potential of the three nanocellulose suspensions was shown in Fig.2(e). The results showed the highest negative charge on the surface of TCNF (-57.2 mV) due to the increased content of negatively charged carboxyl groups and the electric repulsion between the negative charges reduced the flocculation effect of fibrils and improved the stability of TCNF suspension, which was consistent with the result in Fig.2(b) [35]. The FT-IR spectra of the three nanocelluloses was showed in Fig.2(f). The characteristic peaks at 3420 cm^{-1} and 1060 cm^{-1} were respectively attributed to the stretching vibrations of -OH and the asymmetric stretching vibration of C-O-C bonds, indicating that the chain structure of nanocellulose remained intact [36]. The peaks at 2918 cm^{-1} and 1630 cm^{-1} were respectively

attributed to the asymmetric stretching vibration of C-H bonds and the asymmetric stretching vibration of carboxylate groups (COO^-). The FT-IR spectra of TCNF showed a weakened peak at 2918 $cm^{-1}$and an intensified peak at 1630 cm^{-1}, resulting from the occurrence of TEMPO oxidation, which converting the primary hydroxyl oxygen of C_6 into carboxyl groups. The XRD patterns of the three nanocelluloses were showed in Fig.2(g), all the samples displayed diffraction peaks at 16.2° (101) and 22.5° (200), corresponding to the crystallographic structure of cellulose I, confirming that the crystal structure of cellulose remained unchanged during the enzymatic hydrolysis, TEMPO oxidation and mechanical treatments [37]. The TG and DTG curves of the three nanocellulose were showed in Fig.2(h) and Fig.2(i). All nanocellulose samples underwent three weight loss stages, and the weight loss below 200 °C in the first stage mainly due to the evaporation of water. The pyrolysis of cellulose mainly occurred at temperature ranged from 200 °C to 350 °C, and the temperatures corresponding to the maximum thermal degradation rate were respectively 325 °C for CNF, 310 °C for ECNF, and 308 °C for TCNF, that is, TCNF degraded at a lower temperature than CNF and ECNF and had a poorer thermal stability. The result was related to the smaller fiber size and a lower degree of polymerization of TCNF resulting from TEMPO oxidation.

3.2. Oil absorption capacity and oil-water separation efficiency of the nanocellulose aerogels

Oil absorption capacity and oil-water separation efficiency of the three nanocellulose aerogels were showed in Fig.3. Fig.3(a) showed that the oil absorption capacity of the nanocellulose aerogels was greatly improved after SAC modification. The order of oil absorption capacity of the SAC modified nanocellulose aerogels were TCNF > ECNF > CNF, and the oil absorption capacity of the SAC modified TCNF aerogel was as high as 53.3 $g \cdot g^{-1}$ due to its uniform pore structure and large specific surface area. Fig.3(b) showed that SAC modified TCNF aerogel had the highest oil-water separation efficiency, reaching up to 99.8 %, indicating it was an ideal oil-water separation material.

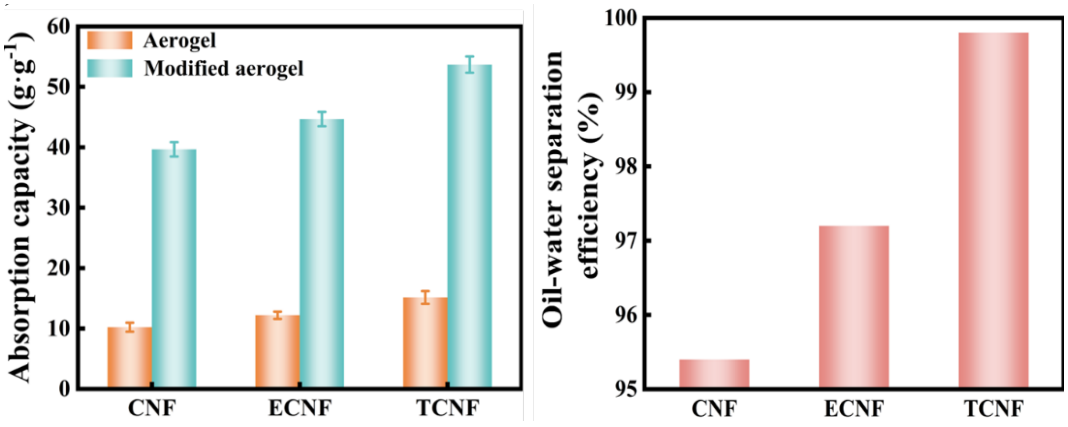

(a) *(b)*

Fig. 3. Oil absorption capacity and oil-water separation efficiency of nanocellulose aerogels (a) Oil absorption capacity before and after SAC modification; (b) Absorption capacity and oil-water separation efficiency of the SAC modified nanocellulose aerogels.

3.3. Morphologies of SAC-TCNF/PVA composite aerogels

The morphological characteristics of the composite aerogels were showed in Fig.4(a). All samples formed self-assembly lamellar structures via cellulose fiber aggregation during freeze-drying, and the final porous architecture was influenced by ice crystal growth direction [38]. Compared to TCNF aerogels, the SAC-modified TCNF aerogels showed smaller pore sizes, higher density, more uniform pore distribution, and increased surface roughness, and as the increase of PVA content, the aerogels developed a progressively denser honeycomb-like structure, also showed a more uniform pore distribution. The addition of PVA inhibited the self-aggregation of nanocelluloses and altered the arrangement of fibers and the growth direction of ice crystal [19].

Furthermore, the increased PVA content provided more hydroxyl reaction sites and promoted SAC esterification, enhancing the surface roughness of TCNF/PVA aerogels. These synergistic effects promoted the formation of dense and porous aerogels with the reduced wettability, endowing SAC-TCNF/PVA aerogels with oil-water separation capability.

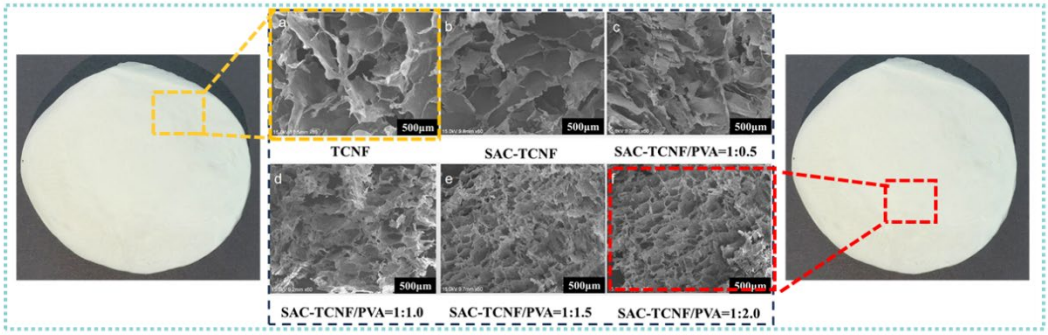

(a)

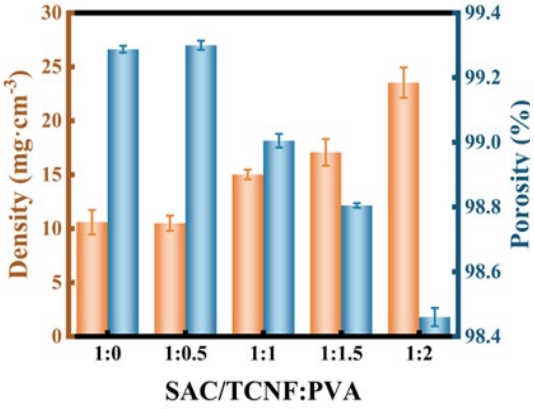

(b)

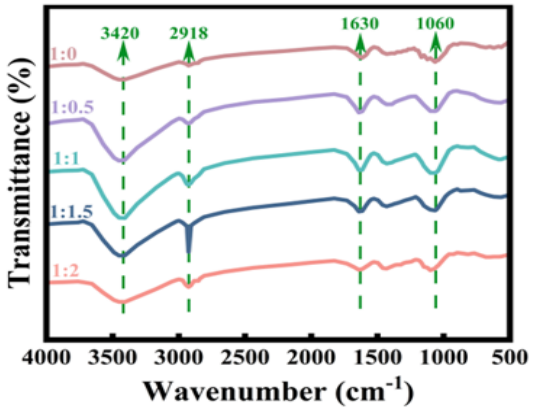

(c)

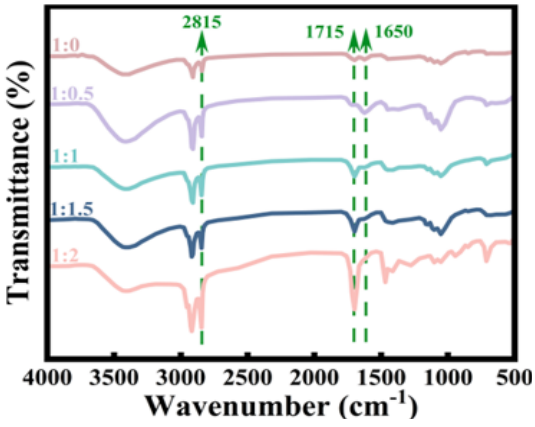

(d)

Fig. 4. Morphology of composite aerogels (a) SEM image of aerogels with TCNF and different TCNF/PVA ratios; (b) Density and porosity of SAC modified TCNF/PVA ratios; (c) Infrared spectra of composite aerogels with different TCNF/PVA ratios; (d) Infrared spectra of composite aerogels with different SAC modified TCNF/PVA ratios.

The influence of the PVA content on the density and porosity of the SAC-TCNF/PVA composite aerogels were showed in Fig.4(b). The density of the SAC-TCNF/PVA aerogels gradually increased with the increase of PVA content, while the porosity gradually decreased. When the ratio of TCNF to PVA was 1:0.5, the density and porosity of the SAC-TCNF/PVA aerogel had no significant change, however, as the ratio of TCNF to PVA increased to 1:2, the density of SAC-TCNF/PVA aerogels increased greatly to 23.53 mg·cm^{-3}, while the porosity decreased slowly to 98.46%. The inter-fibrillar bonding in SAC-TCNF/PVA aerogels was enhanced via the crosslinking effect of PVA, and the results were consistent with the SEM images in Fig.4(a) [38].

The FT-IR spectra of TCNF/PVA and SAC- TCNF/PVA aerogels were respectively showed in Fig.4(c) and Fig.4(d). The characteristic absorption peaks at 3420 cm^{-1}, 2918 cm^{-1}, 1630 cm^{-1} and 1060 cm^{-1} were respectively assigned to the O-H, C-H, COO^- and C-O-C of TCNF aerogels, and there was no new peak appeared as shown in Fig.4(c), indicating the introduction of PVA kept the chemical structure of nanocellulose unchanged, and the intensity of hydroxyl peak at 3420 cm^{-1} increased proportionally with PVA content due the physical crosslinking effect between TCNF and PVA through by hydrogen bonds. Fig.4(d) showed that there were two new characteristic peaks at 2815 cm^{-1} and 1715 cm^{-1}, which were respectively attributed to the stretching vibrations of -CH_2- and the stretching vibrations of C=O, indicating successful esterification between TCNF and stearic acid. The peaks at 1715 cm^{-1} and 2815 cm^{-1} were intensified when the ratio of TCNF to PVA was 1:2 due to the increased hydroxyl groups provided additional esterification sites for stearyl chloride, thereby introducing more long chain fatty acids [39]. The absorption peak at 1650 cm^{-1} corresponding to the bending vibration of O-H weakened with the increase of PVA, and even disappeared when the ratio of TCNF to PVA was 1:2, indicating substantially improved hydrophobic properties of SAC-TCNF/PVA aerogels.

3.4. The hydrophobic property of SAC-TCNF/PVA composite aerogels

The WCA of TCNF aerogel and TCNF/PVA composite aerogels before and after modification were showed in Fig.5.

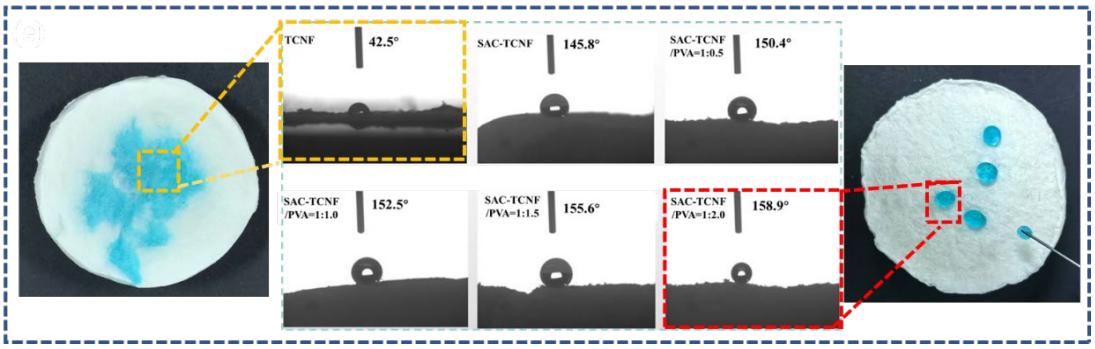

Fig. 5. WCA of composite aerogels before and after SAC modification.

The WCA of TCNF aerogel was only 42.5°, showing hydrophilic properties. After modification with SAC, the WCA of SAC-TCNF aerogel rose sharply to 145.8°, displaying a hydrophobic state. The WCA of the SAC-TCNF/PVA composite aerogel reached 150.4° when the ratio of TCNF to PVA was 1:0.5, achieving a superhydrophobic state. The WCA of the SAC-TCNF/PVA composite aerogels further increased with the increase of PVA content, and reached 158.9° when the ratio of TCNF to PVA was 1:2. The higher PVA content provided more esterification sites for stearoyl chloride and introduced more nonpolar long chain fatty acid, and the results were confirmed by the FT-IR analysis [40].

3.5. Thermal stability analysis of SAC-TCNF/PVA composite aerogels

The TG and DTG curves of the SAC-TCNF/PVA composite aerogels were showed in Fig.6(a) and Fig.6(b).

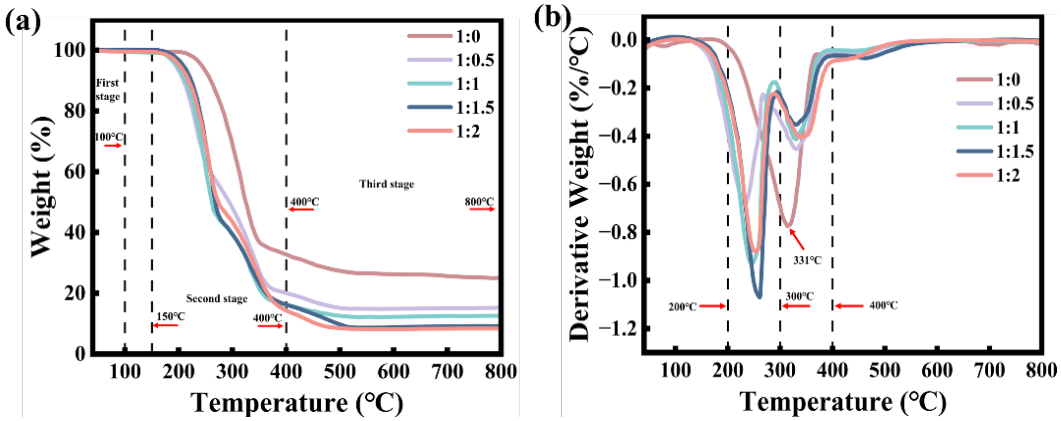

Fig. 6. (a)TG and (b) DTG curves of SAC-TCNF/PVA composite aerogels.

The first weight loss occurred when the aerogels were heated from room temperature to 100 ℃, which was attributed to the evaporation of water in the samples. A rapid decrease of weight was observed at the temperature ranged from 150 ℃ to 400 ℃, and it was mainly caused by the pyrolysis of cellulose molecular and the decomposition of TCNF-PVA crosslinking network. For TCNF aerogel, there was only one maximal weight loss rate peak at the temperature of 331 ℃, which corresponding to the pyrolysis of cellulose molecular, while there were two weight loss rate peaks in the TCNF/PVA composite aerogels, where the peak at the temperature of 200 ℃-300 ℃ corresponding to the pyrolysis of cellulose molecular and the peak at temperature of 300 ℃-400℃ was attributed to the decomposition of TCNF-PVA crosslinking network. And the weight loss of aerogel was very low when the temperature was above 400 ℃. The residual mass of SAC-TCNF/PVA composite aerogels at 800 ℃ were lower than that of SAC-TCNF aerogel, and it was attributed to the introduction of more SAC molecules and -CH_2- chains by the addition of PVA, thereby promoting thermal degradation and reducing residue [15].

3.6. Elastic recovery rate and oil-water separation performance of SAC-TCNF/PVA composite aerogel

The SAC-TCNF/PVA composite aerogel was put into oil-water mixture, and oil absorption process was showed in Fig.7(a). It could be seen that the SAC-TCNF/PVA composite aerogel floated on the surface of the oil-water mixture without sedimentation due to its low density and hydrophobicity. After few seconds, the SAC-TCNF/PVA composite aerogel was filled with edible oil and reached saturation, and the edible oil was disappeared from the oil-water mixture, indicating the excellent oil-water separation effect of the SAC-TCNF/PVA composite aerogel.

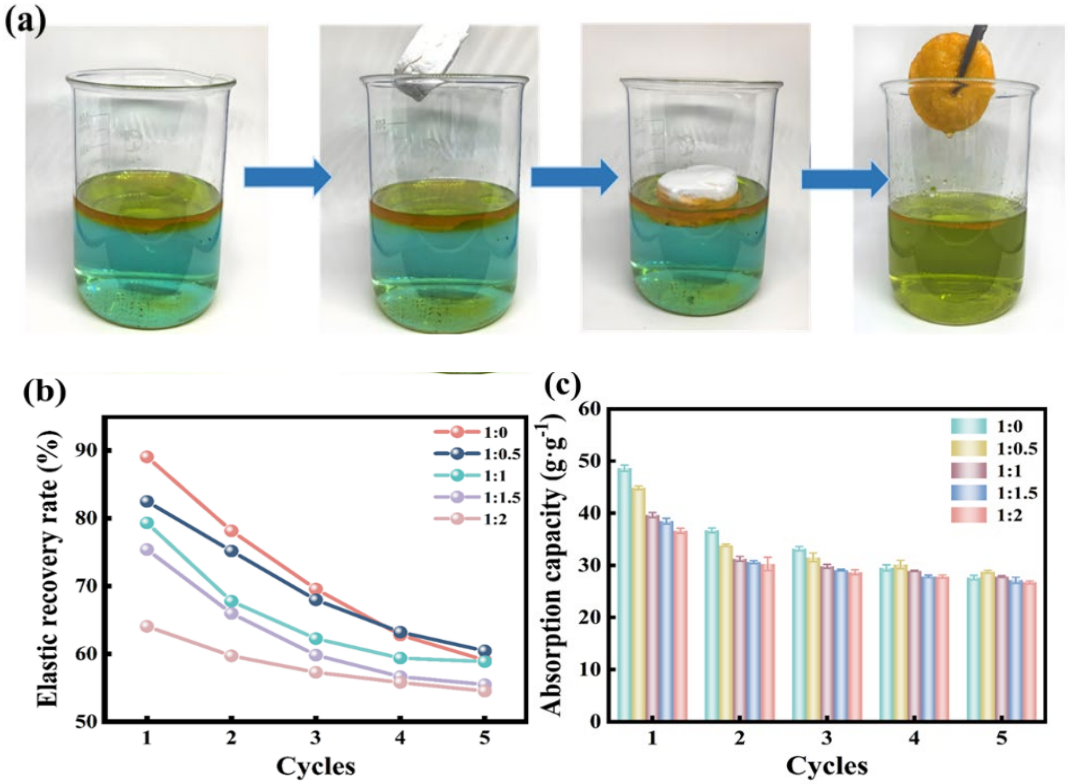

Fig. 7. Elastic recovery rate and Oil-water separation performance of SAC-TCNF/PVA composite aerogel (a)Edible oil absorption process of SAC-TCNF/PVA composite aerogel; (b)The change of elastic recovery rate of modified composite aerogels; (c)Cyclic oil absorption capacity of SAC-TCNF/PVA composite aerogel.

The elastic recovery rate of SAC-TCNF/PVA composite aerogels over five compression cycles were showed in Fig.7(b). The results demonstrated that the SAC-TCNF/PVA aerogel exhibited the highest elastic recovery rate after five compression cycles when the ratio of TCNF to PVA was 1:0.5, and the elastic recovery rate decreased with the increase of PVA content. The increase of PVA increased the density and reduced the porosity of the TCNF/PVA composite aerogels, and SAC modification further promoted the formation of tighter three-dimensional network, which restricting the deformation of SAC-TCNF/PVA composite aerogels. Considering the requirements of high porosity and good elastic recovery rate, the optimal ratio of TCNF to PVA was 1:0.5. The cyclic oil absorption performance of the SAC-TCNF/PVA composite aerogels was showed in Fig.7(c). The results showed that of the oil absorption capacity of the SAC-TCNF aerogel declined rapidly with the progress of the cyclic oil absorption test. It might be attributed to the loose binding between nanofibrils of TCNF aerogel, which was easily damaged during recycling, resulting in a decrease in oil absorption capacity. The results also revealed that the oil absorption capacity of SAC-TCNF/PVA composite aerogels progressively decreased with the increase of PVA content, and the fifth cyclic oil absorption capacity of the SAC-TCNF/PVA composite aerogels with different ratio of TCNF to PVA from 1:0 to 1:2 were 29.8 $g \cdot g^{-1}$, 31.6 $g \cdot g^{-1}$, 30.4 $g \cdot g^{-1}$, 30.0 $g \cdot g^{-1}$ and 29.6 $g \cdot g^{-1}$, respectively. Notably, the SAC-TCNF/PVA composite aerogel had the maximum oil absorption capacity in the fifth cycle when the ratio of TCNF to PVA was 1:0.5. The reason was that high PVA content enhanced molecular crosslinking, reduced pore size, and consequently weakened oil absorption performance.

4. Conclusions

Three kinds of nanocellulose were prepared respectively by high-pressure homogenization, combining enzymatic pretreatment with high-pressure homogenization and TEMPO-mediated oxidation with high-pressure homogenization, and the corresponding nanocellulose aerogels were prepared and hydrophobically modified by SAC. The characteristics of the nanocelluloses were investigated by AFM, FT-IR, Zeta potential, TSI, XRD and TGA, and the nanocellulose aerogels were compared according to their oil absorption capacity and oil-water separation efficiency. The results showed that the TEMPO-oxidized nanocellulose (TCNF) exhibited the smallest diameter, the highest zeta potential value (-57.2 mV), the best uniformity and dispersion stability, and the SAC-TCNF aerogel had the optimal oil absorption capacity and oil-water separation efficiency.

In order to further improve the physical properties of the SAC-TCNF aerogel, SAC-TCNF/PVA composite aerogels with different ratios of TCNF to PVA were prepared using PVA as the crosslinking agent. The results revealed that SAC-TCNF/PVA composite aerogel maintained optimal characteristics with a density of 15.2 $mg \cdot cm^{-3}$ and a porosity of 99.0 % when the ratio of TCNF to PVA was 1:0.5, exhibiting superhydrophobicity with a WCA of 150.4°, high elastic recovery rate of 59.5 % after five rebound tests, high cyclic oil absorption capacity of 31.6 $g \cdot g^{-1}$ in the fifth cycle, which was 69.7 % of the initial oil absorption capacity. This study provides an innovative method to solve the problem of oil pollution in water by the utilization of high-performance oil-water separation nanocellulose composite aerogel.

Acknowledgments

This work was financially supported by the Science and Technology Planning Project of Quzhou City (No.2024Z008).

References

[1] L. H. Mao, Y. Lian, Y. L. Ma, et al., Chemical Engineering Science, 298: 120389 (2017); https://doi.org/10.1016/j.ces.2024.120389
[2] S. Shao, Y. Li, T. Lü. Water, 11(10): 1993 (2019); https://doi.org/10.3390/w11101993
[3] T. Diwan, M. H. Al-Furaiji, Z. N. Abudi, et al., The Canadian Journal of Chemical Engineering, 103(3): 1375-1399 (2025); https://doi.org/10.1002/cjce.25449
[4] X. Guo, Y. X. Zhang, J. Li, et al., Advanced Fiber Materials, 6: 1669-1709 (2024); https://doi.org/10.1007/s42765-024-00440-6
[5] J. Kim, G. Kim, S. Baek, et al., Journal of Porous Materials, 29(3): 861-868 (2022); https://doi.org/10.1007/s10934-022-01215-3
[6] W. W. Guo, S. Chen, F. W. Liang, et al., International Journal of Biological Macromolecules, 246: 125343 (2023); https://doi.org/10.1016/j.ijbiomac.2023.125343
[7] P. M. Tu, D. N. C. Vy, L. T. Ngan, et al., Biomass Conversion and Biorefinery, 14(17): 20089-20103 (2024); https://doi.org/10.1007/s13399-023-04176-y
[8] Y. M. Chen, L. Zhang, Y. Yang, B. Pang, et al., Advanced Materials, 33(11): 2005569 (2021); https://doi.org/10.1002/adma.202005569
[9] Z. X. Wu, S. Z. Shu, X. L. Hu, et al., International Journal of Biological Macromolecules, 305: 141173 (2025); https://doi.org/10.1016/j.ijbiomac.2025.141173
[10] Y. Q. Guo, J. C. Zhang, S. Y. Wang, et al., Polymers, 17(3): 273 (2025); https://doi.org/10.3390/polym17030273
[11] K. H. Zhang, Y. H. Su, H. Xiao. BioResources, 15(3): 6636 (2020); https://doi.org/10.15376/biores.15.3.6636-6647
[12] X. Zhang, J. Guo, Y. Liu, et al., Materials Today Chemistry, 27: 101346 (2023); https://doi.org/10.1016/j.mtchem.2022.101346

[13] A. Isogai, Y. Zhou, Current Opinion in Solid State and Materials Science, 23(2): 101-106 (2019); https://doi.org/10.1016/j.cossms.2019.01.001
[14] Y. Mo, X.Y. Huang, M. Yue, et al., RSC advances, 14(26): 18247-18257 (2024); https://doi.org/10.1039/D4RA01412J
[15] S. Mueller, J. Sapkota, A. Nicharat, et al., Journal of Applied Polymer Science, 132(13): 41740 (2015); https://doi.org/10.1002/app.41740
[16] Z. Wang, W. K. Zhu, R. Z. Huang, et al., Polymers, 12(11): 2583 (2020); https://doi.org/10.3390/polym12112583
[17] L. Mendoza, T. Gunawardhana, W. Batchelor, et al., Journal of colloid and interface science, 525: 119-125 (2018); https://doi.org/10.1016/j.jcis.2018.04.077
[18] X. Q. Chen, X. Y. Deng, W. H. Shen, et al., BioResources, 7(3): 4237-4248 (2012); https://doi.org/10.15376/biores.7.3.4237-4248
[19] C. Gong, J. P. Ni, C. Tian, et al., International Journal of Biological Macromolecules, 172: 573-579 (2021); https://doi.org/10.1016/j.ijbiomac.2021.01.080
[20] S. Takeshita, A. Konishi, Y. Takebayashi, et al., Biomacromolecules, 18(7): 2172-2178 (2017); https://doi.org/10.1021/acs.biomac.7b00562
[21] Y. H. Li, X. H. He, P. T. Liu, Journal of Polymers and the Environment, 31(6): 2380-2387 (2023); https://doi.org/10.1007/s10924-023-02768-3
[22] E. B. Yahya, S. S. Elarbash, S. B. Moussa, et al., Industrial Crops and Products, 221: 119358 (2024); https://doi.org/10.1016/j.indcrop.2024.119358
[23] C. L. He, J. Y. Huang, S. H. Li, et al., ACS Sustainable Chemistry & Engineering, 6(1): 927-936 (2018); https://doi.org/10.1021/acssuschemeng.7b03281
[24] F. Rafieian, M. Hosseini, M. Jonoobi, et al., Cellulose, 25: 4695-4710 (2018); https://doi.org/10.1007/s10570-018-1867-3
[25] M. Takemoto, Y. Tokudome, D. Noguchi, et al., Langmuir, 36(32): 9436-9442 (2020); https://doi.org/10.1021/acs.langmuir.0c01292
[26] T. L. Zhou, H. W. Choi, G. Jabbour, ACS omega, 9(20): 21798-21804 (2024); https://doi.org/10.1021/acsomega.3c08062
[27] W. Y. Liu, W. X. Wang, R. Fan, et al., Journal of Polymer Research, 31(12): 347 (2024); https://doi.org/10.1007/s10965-024-04197-9
[28] J. K. Ogunjobi, A. I. Adewale, S. A. Adeyemi, Heliyon, 9(1): e13104 (2023); https://doi.org/10.1016/j.heliyon.2023.e13104
[29] X. D. Hu, S. S. Zhang, B. Yang, et al., Applied Surface Science, 640: 158299 (2023); https://doi.org/10.1016/j.apsusc.2023.158299
[30] Z. C. Lou, Y. Zhang, Y. J. Li, et al., Journal of Materials Research and Technology, 24: 10005-10026 (2023); https://doi.org/10.1016/j.jmrt.2023.05.176
[31] H. F. He, L. Liu, H. L. Ding, et al., ACS Nano, 18(52): 35465-35479 (2024); https://doi.org/10.1021/acsnano.4c12853
[32] M. T. Zhang, M. Su, Y. J. Qin, et al., 2D Materials, 10(2): 24007 (2023); https://doi.org/10.1088/2053-1583/acc3aa
[33] G. Banvillet, C. Grange, D. Curtil, et al., Cellulose, 30(4): 2123-2146 (2023); https://doi.org/10.1007/s10570-022-05016-4
[34] L. L. Qin, Y. Y. Zhou, Y. B. Lei, et al., Digest Journal of Nanomaterials and Biostructures, 19(3): 1277-1290 (2024).
[35] C. Tang, H. Chen, Z. Shi, et al. Cellulose, 31(18): 10785-10800 (2024); https://doi.org/10.1007/s10570-024-06262-4
[36] P. Sharma, S. Hicks, A. R. Ruggiero, et al., Cellulose, 32(2): 887-902 (2025); https://doi.org/10.1007/s10570-024-06328-3
[37] J. Zhang, Y. H. Li, X. X. Wang, et al., International Journal of Biological Macromolecules, 283: 137984 (2024); https://doi.org/10.1016/j.ijbiomac.2024.137984
[38] Z. Y. Xu, X. D. Jiang, H. Zhou, et al., Cellulose, 25: 1217-1227 (2018); https://doi.org/10.1007/s10570-017-1619-9
[39] P. Phanthong, P. Reubroycharoen, S. Kongparakul, et al., Carbohydrate polymers, 190: 184-189 (2018); https://doi.org/10.1016/j.carbpol.2018.02.066
[40] Y. X. Zhen, C. C. Peng, H. M. Gao, et al., Biomacromolecules, 25(12): 7767-7776 (2024); https://doi.org/10.1021/acs.biomac.4c01082